Numerical Simulation of Shock Induced Turbulence in a Nozzle flow

Mohammad Ali Jinnah[1]

***Abstract*— In the present paper, a study has been conducted to investigate the shock induced turbulent flow fields and shock/turbulent-boundary layer interaction at the nozzle divergent. Experimental photographs and numerical images are used to investigate on laminar flow structures, transition phenomena, flow separation line as well as viscous boundary layer separation, turbulence structure development and shock/turbulent-boundary layer interaction. It is observed that transition from laminar to turbulent flow separation is shown earlier at the nozzle divergent for the weaker shock wave propagation and the fully developed turbulence is appeared with unsteady flow fluctuations at the end of the nozzle divergent. It is found that the pressure downstream of the separation point showed an unsteady behavior with strong oscillations, and finally jumped to values quite above the ambient pressure. By solving the 2D Navier-Stoke's equations with *k-ε* turbulence model, all turbulent parameters are determined at the end of the nozzle divergent and it is observed that turbulence intensities are almost uniform at the end of the nozzle divergent where slight decay phenomena are appeared along the downstream direction. The skewness of the velocity fluctuations indicates that the present flow appears to be isotropic at the end of the nozzle divergent**

***Index Terms*— Shock wave; Turbulence; Nozzle flow; Flow separation; Boundary layer.**

I. Introduction

Shock induced turbulence and shock/turbulent boundary layer interaction at the divergence part of the nozzle are the major observations in the present work. Due to acceleration of the shock speed at the divergence part, tremendous viscous flow separations as well as fully developed turbulent field are appeared where the shock induced flow fields are becoming supersonic. Separation of supersonic flow in a convergent–divergent nozzle is a basic fluid-dynamics phenomenon that occurs in a variety of aerospace applications. The flow separation in a supersonic stream is associated with the generation of an oblique shock wave, the separation-shock wave, also allowing the supersonic stream to recover to the ambient pressure value.

Computational studies of two-dimensional over-expanded nozzles by Wilmoth and Leavitt [1] and by Hamed and Voyatzis [2, 3] assessed the accuracy of turbulence models for predicting the flow field and thrust performance. The works agreed on the basic structure of the separation shock, which consisted of the incident shock, Mach stem (normal shock), and reflected shock. Thrust predictions were in good agreement with experiments, except at pressure ratios associated with separated flow. A combined experimental and computational work by Hunter [4] offered one of the most comprehensive treatments of this flow. Hunter claimed that this transition was not the result of markedly different onset conditions or stronger shock-boundary layer interaction, but instead came about through the natural tendency of an over-expanded nozzle flow to detach and reached a more efficient thermodynamic balance.

From a numerical point of view, several studies were undertaken to simulate nozzle flow transients. Prodromou et al. [5] and Igra et al. [6] carried out Euler simulations of the two-dimensional plane reflection nozzle of Amann [7] with rounded and sharp-edged inlet respectively. On the other hand, Jacobs [8], Tokarcik-Polsky et al. [9] and Saito et al. [10] presented numerical simulations of the same type of nozzle, including viscous effects. It may be concluded from these studies that inviscid computations satisfactorily predict the main flow features (namely the primary and secondary shock waves, multiple shock wave reflections and slip surfaces). Nevertheless, the investigation of phenomena connected with boundary layer separation requires viscous simulations. Concerning rocket nozzles, Chen et al. [11], among others, examined the flow structures of the start-up and shut-down processes using a Navier Stokes solver with a turbulence model. The configuration they studied was a sub-scale nozzle of a J-2S rocket engine. Later, Nasuti et al. [12] and [13] simulated the flow transients during the start-up of the Vulcain nozzle. Both inviscid and viscous laminar flow models were considered and permitted to demonstrate that very peculiar flow field configurations, which are characterized by two main vertical regions, may occur during the start-up of the nozzle. A two-dimensional and fully turbulent, unsteady and separated transonic flow over a thick circular arc foil was studied and computed with help of an algebraic turbulence model by Seegmiller *et al.* [14] and compared with experimental data. Chen *et al.* [15] measured the natural oscillations of a shock wave in separated diffuser flow, while Liou and Coakley [16] compared measured self-excited and forced fluctuations of weak and strong shock waves with numerical computations based on thin-layer Navier-Stokes equations with the low-Reynolds k-ω^2 two-equation turbulence model. Shock buffeting over bi-circular airfoil was computed and compared with experiment by Arnone *et al.* [17], on the basis of Navier-Stokes equations with an algebraic Baldwin and Lomax turbulence model. Gerolymos *et al.* [18] investigated the influence of three-dimensional effects on the transonic flow in a nozzle by means of a k-ε turbulence closure. More recently, Bron *et al.* [19] explored non-linear interactions in a two-dimensional nozzle configuration using the Wilcox k-ω turbulence model. Very interesting results of the Reynolds number's influence on the unsteady flow through a critical nozzle had been presented by Setoguchi *et al.* [20]. All previous work concerning forced shock wave oscillations in nozzles underline the fact that the amplitude of the shock

[1] Islamic University of Technology (IUT) BoardBazar, Gazipur-1704, Bangladesh *E*-mail Address: *jinnah@iut-dhaka.edu*

movement depends on both the amplitude and frequency of imposed back pressure changes.

In the present research works, a turbulent region is selected at the divergent part of the nozzle where the throat effects are negligible. Due to shock wave propagation through divergent part, the shock/turbulent boundary layer interaction starts and for further movement of the shock wave, the shock wave speed is accelerated where tremendous viscous flow separations as well as fully developed turbulent field are appeared. In the present computation, the 2D Navier-Stoke's equations using k-ε turbulence model, are solved by shock capturing method where for more accurate solutions, the grid adaptation techniques are used. All turbulent parameters are computed along the centerline of the selected region at the divergence part of the nozzle.

II. Numerical simulation

A. Governing Equations

The two-dimensional unsteady, compressible, Reynolds-Averaged Navier-Stokes (RANS) equations with k-ε turbulence model are solved by shock capturing method. Without external forces and heat sources, the conservative form of non-dimensionalized governing equation in two-dimensional Cartesian coordinate system is

$$\frac{\partial Q}{\partial t}+\frac{\partial (F-Fv)}{\partial x}+\frac{\partial (G-Gv)}{\partial y}=S(Q)$$

where
$Q = [\ \rho, \rho u, \rho v, e, \rho k, \rho\varepsilon\ ]$,
$F = [\ \rho u, \rho u^2, \rho uv, u(e+p)\ , \rho uk, \rho u\varepsilon\ ]$,
$G = [\ \rho v, \rho uv, \rho v^2, v(e+p)\ , \rho vk, \rho v\varepsilon\ ]$,
$Fv = [\ 0, \tau_{xx}, \tau_{xy}, u\tau_{xx}+v\tau_{xy}-q_x, k_x, \varepsilon_x\ ]$,
$Gv = [\ 0, \tau_{xy}, \tau_{yy}, u\tau_{xy}+v\tau_{yy}-q_y, k_y, \varepsilon_y\ ]$.

Here Q is the vector of conservative variables which contains mass, momentum and energy. All variables are calculated in per unit volume. ρ is taken as the mass per unit volume. Two momentum terms in two-dimensional Cartesian coordinates system are ρu, and ρv per unit volume. Total energy, e, turbulent kinetic energy, ρk and turbulent dissipative energy, $\rho\varepsilon$ are the energy terms per unit volume in these computations. F and G are the two inviscid flux vectors in x- and y- axis respectively. Similarly Fv and Gv are the two viscous flux vectors in x- and y- axis respectively. Each flux vectors contain mass flux, momentum flux and energy flux. ρu is the mass flux and ρu^2, ρuv are the momentum flux and $u(e+p)$, ρuk, $\rho u\varepsilon$ are the energy flux in the x-axis. Similarly ρv is the mass flux and ρuv, ρv^2 are the momentum flux and $v(e+p)$, ρvk, $\rho v\varepsilon$ are the energy flux in the y-axis. Also ρ is the fluid density and u and v are velocity components in each direction of Cartesian coordinates. While e is the total energy per unit volume, pressure p can be expressed by the following state equation for ideal gas:

$$p=(\gamma-1)[e-\tfrac{1}{2}\rho(u^2+v^2)]$$

where γ is the ratio of specific heats.

From the relationship between stress and strain and assumption of stokes, non-dimensional stress components are as follows:

$$\tau_{xx}=\frac{\mu}{\mathrm{Re}}\ \tfrac{2}{3}\ (2.\frac{\partial u}{\partial x}-\frac{\partial v}{\partial y}),$$

$$\tau_{yy}=\frac{\mu}{\mathrm{Re}}\ \tfrac{2}{3}\ (2.\frac{\partial v}{\partial y}-\frac{\partial u}{\partial x}),$$

$$\tau_{xy}=\frac{\mu}{\mathrm{Re}}\ (\frac{\partial v}{\partial x}+\frac{\partial u}{\partial y}),$$

$$k_x=\frac{1}{\mathrm{Re}}\ (\mu_l+\frac{\mu_t}{\sigma_k})\frac{\partial k}{\partial x},$$

$$\varepsilon_x=\frac{1}{\mathrm{Re}}\ (\mu_l+\frac{\mu_t}{\sigma_\varepsilon})\frac{\partial \varepsilon}{\partial x},$$

$$k_y=\frac{1}{\mathrm{Re}}\ (\mu_l+\frac{\mu_t}{\sigma_k})\frac{\partial k}{\partial y},$$

$$\varepsilon_y=\frac{1}{\mathrm{Re}}\ (\mu_l+\frac{\mu_t}{\sigma_\varepsilon})\frac{\partial \varepsilon}{\partial y}.$$

The expression of laminar viscosity is $\mu_l/\mu_o = c_v\ (T/T_o)^{1.5}$ where μ_o is the laminar viscosity at the ambient temperature (T_o) and the coefficient, c_v depends on the temperature and the ambient gas. The total viscosity $\mu = \mu_l + \mu_t$ where μ_t is the turbulent eddy viscosity and the expression of turbulent eddy viscosity,

$$\mu_t = c_\mu \rho \frac{k^2}{\varepsilon}.$$

The element of heat flux vectors are expressed by Fourier law of heat conduction as

$$q_x=\frac{k_c}{\mathrm{Re}}\ \frac{\partial T}{\partial x},\ \ q_y=\frac{k_c}{\mathrm{Re}}\ \frac{\partial T}{\partial y}$$

where T is the temperature, k_c is the thermal conductivity and it expresses by $k_c = k_l + k_t$. The expression of the thermal conductivity of the laminar part is $k_l/k_o = c_k\ (T/T_o)^{1.5}$ where k_o is the thermal conductivity at the ambient temperature and the value of the coefficient, c_k depends on the temperature and the ambient gas. The expression of the thermal conductivity of the turbulent part is

$$k_t = c_{tk}\ \mu_t \big/ \mathrm{Pr}$$

where the value of the coefficient, c_{tk} depends on the temperature and the ambient gas. Pr is the Prandtl number based on characteristic values. The Reynolds number of the flow is defined by $\mathrm{Re} = (\rho_c u_c l_c/\mu_o)$ where ρ_c, u_c, l_c and μ_o are respectively a characteristic density, a characteristic velocity, a characteristic length and the viscosity of the fluid.

The source term $S(Q)$ of k-ε turbulence model is given by,

$S(Q) = [\ 0, 0, 0, 0, 0, P_k-\rho\varepsilon-D_k,\ (c_{\varepsilon 1}.P_k-c_{\varepsilon 2}.\rho\varepsilon)\ \frac{\varepsilon}{k}\ ]$

where the production term P_k, which is the two-dimensional formulation, is given in Cartesian coordinates as:

$$P_k=\{\ 2\ \mu_t\frac{\partial u}{\partial x}-\tfrac{2}{3}\ [\ \rho k+\mu_t(\frac{\partial u}{\partial x}+\frac{\partial v}{\partial y})]\}\frac{\partial u}{\partial x}+$$

$$\{\ 2\ \mu_t\frac{\partial v}{\partial y}-\tfrac{2}{3}\ [\ \rho k+\mu_t(\frac{\partial u}{\partial x}+\frac{\partial v}{\partial y})]\}\frac{\partial v}{\partial y}+\mu_t(\frac{\partial u}{\partial y}+\frac{\partial v}{\partial x})^2$$

and the destruction term D_k is given as $D_k = \dfrac{2\rho}{\gamma.T}k\varepsilon$.

The mass average initial turbulent kinetic energy and homogeneous component of initial turbulent kinetic energy

dissipation rate are defined by as:

$$k_o = \frac{1}{2}\, c_t^2\,(u^2+v^2) \quad \text{and} \quad \varepsilon_o = c_m\, k^2\, \frac{\mathrm{Re}}{100}$$

The various constants in the k-ε turbulence model are listed as follows:

$c_\mu = 0.09$, $c_t = 0.03$, $c_m = 0.09$, $c_{\varepsilon 1} = 1.45$, $c_{\varepsilon 2} = 1.92$, $\sigma_k = 1.00$, $\sigma_\varepsilon = 1.30$

The following characteristics values are used for non-dimensionalized in these computations: Characteristics temperature = 298.00K, Characteristics length = 0.0010 m, Characteristics pressure = 101000 Pascal, Universal Gas constant = 8.31451, Moleculer weight = 0.029, Ratio of specific gas constant = 1.4, Characteristics velocity = 292.30 m/s, Characteristics density = 1.1821 kg/m3, Characteristics time = 3.4 μsec, Thermal conductivity at 0oC = 0.02227 W/m-K, Fluid viscosity at 0oC = 1.603E-05 Pa.S, Prandtl number = 0.722, Reynolds number = 21546.

B. Numerical schemes

The governing equations described above for compressible viscous flow are discretized by the finite volume method. A second order, upwind Godunov scheme of Flux vector splitting method is used to discretize the inviscid flux terms and MUSCL-Hancock scheme is used for interpolation of variables. Central differencing scheme is used in discretizing the viscous flux terms. HLL Reimann solver is used for shock capturing in the flow. Two equations for k-ε turbulence model are used to determine the dissipation of turbulent kinetic energy and ε the rate of dissipation. The k and ε equations, each contains nonlinear production and destruction source terms, which can be very large near the solid boundaries.

C. Grid Systems and Grid Adaptation

Two-dimensional quadrilateral cells with adaptive grid systems are used in these computations. In this grid systems, the cell-edge data structures are arranged in such a way that each cell contains four faces which are sequence in one to four and each face indicates two neighboring cell that is left cell and right cell providing all faces of a cell are vectorized by position and coordinate in the grid systems. The initial minimum size of the cell is 0.154 mm^2 and the maximum size of the cell before adaptation is 4.75 mm^2 which are shown in Fig.1.

The grid adaptation is one of the improved and computational time saving techniques, which is used in these computations. The grid adaptation is performed by two procedures one is refinement procedure and another is coarsening procedure. The refinement and coarsening operations are handled separately in computation. The criterion used for grid adaptation is based on the truncation error (ϵ_T) of the Taylor series expansion of density. In these computations, the value of α_f is used 0.02 and it is problem-independent parameter. The refinement and coarsening operation for any cell depends on ϵ_T value and this ϵ_T value is determined for each face of a cell. The criterion for adaptation for any cell is,

Refinement = maximum ϵ_T of four faces of a cell $> \varepsilon_r$

Coarsening = maximum ϵ_T of four faces of a cell $< \varepsilon_c$

where ε_r and ε_c are the threshold values for refinement and coarsening. In the computations, the values of ε_r are used 0.30~0.34 and the values of ε_c are used 0.26~0.30 and the level of refinement is 5.

In the refinement procedure, the cells are selected for refinement in which every cell is divided into four new sub cells and these new sub cells are arranged in a particular sequence so that these sub cells are used suitably in the data-structure. In the coarsening procedure, the four sub cells, which are generated from the primary cell, are restored into primary cell.

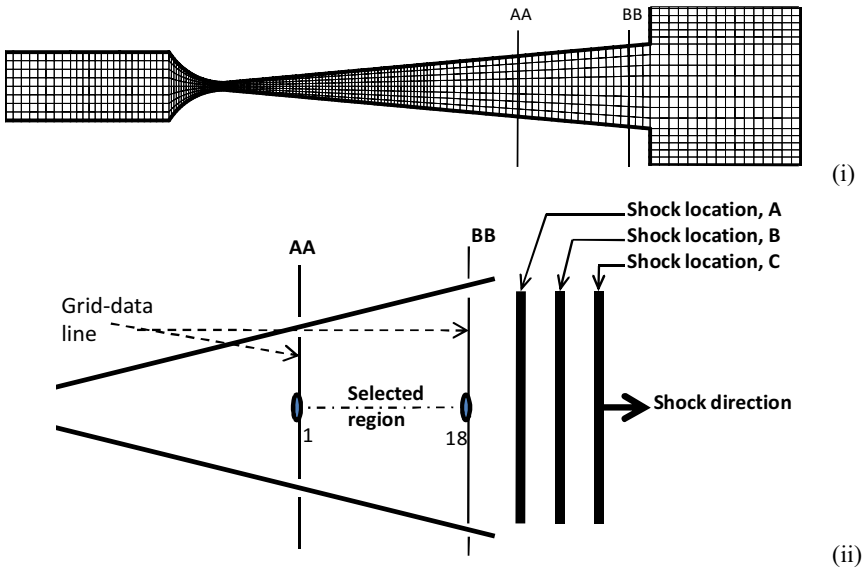

Figure 1: (i) Two- dimensional numerical grids where minimum and maximum cell size are shown (ii) Turbulent region at the divergent part of the nozzle is shown.

A. Initial and Boundary conditions

The two-dimensional domain shown in Fig. 1 (i), is used in these computations. The upstream of incident shock wave is set as an inflow boundary condition, the properties and velocities of which are calculated from Rankine-Hugoniot conditions with incident Mach number and the downstream inflow boundary condition is set as open boundary condition. The wall surfaces are used as solid boundary conditions where the gradients normal to the surface are taken zero. All solid walls are treated as viscous solid wall boundary. The initial temperature of the solid wall is constant and is equal to ambient temperature. No external heat crosses the solid boundary.

III. Results and Discussion

In the present computations, the time-dependent RANS equations with k-ε turbulence model for a compressible fluid are solved by grid adaptation techniques. All relevant turbulence parameters are resolved with k-ε turbulence model and the shock wave is resolved as a solution of the RANS equations with introducing the techniques of shock capturing. HLL-Reimann solver is used for shock capturing in the flow. There has one limitation in DNS of Lee *et al.* [21] where DNS is not valid in a shock wave for M_s >2.00 but the present code is valid for M_s >2.00 by introducing proper shock capturing technique.

For the numerical simulation, the incident shock wave is allowed to propagate through the convergent-divergent nozzle, which is shown in Fig. 1 (i). The shock wave and the gas flow following the shock are passed through the throat of the nozzle. The elementary waves formed by diffraction of the shock at the throat propagate in downstream direction and interacts with the wall of the nozzle and after a short period converge to form again plane, normal shock which is weaker than the incident shock. During wave propagation through divergent part, tremendous viscous flow separations as well as fully developed turbulent field are appeared where the shock induced flow fields are becoming supersonic. To compute turbulent parameters in the turbulent region, a selected turbulent region is taken at the end of the nozzle divergent part, which is shown in Fig.1 (ii). The region between line AA and BB is the selected turbulent region and the centerline along the longitudinal direction (x-axis) of the turbulent region is treated as the centerline of the turbulent region. 18 points of equal spacing are taken on the centerline of the selected region and all turbulent parameters (velocity fluctuations, pressure fluctuations etc.) are computed on these 18 points for the selected region. The lateral lines intersect these 18 points and parallel to the y-axis are treated as grid-data lines and the grids cut by the grid-data lines (lateral lines on 18 points) are the grids on the grid-data lines. The value of any turbulent parameter on the centerline of the selected region is the average value of all the grid values on the grid-data line where the grids near the boundary are not taken into account due to viscous effect.

All the relevant turbulent parameters (velocity fluctuations, pressure fluctuations etc.) are determined along the centerline of selected region for different shock wave position (A, B, C positions) at the outlet of the nozzle divergent. It is possible to observe the behavior of the turbulent field during shock wave movement by considering of different shock positions. The longitudinal distances (x) of any point on the centerline of turbulent regions are determined from the throat of the nozzle.

The wall pressure fluctuations $\langle p\rangle/\Delta P$, are calculated from the computed numerical data where the *RMS* value of wall pressure fluctuations,

$$\langle p\rangle = \sqrt{\frac{\sum_{i=1}^{n}(p_i - P_{av})^2}{n}}$$

Where the average pressure, P_{av} above atmospheric pressure is $(1/n)\sum_{i=1}^{n} p_i$, p_i is the instantaneous pressure and n is the number of grids, cut off by the grid-data line where the grids near the boundary are not taken into account due to viscous effect. Similarly the turbulence intensities, $\langle u\rangle/U_{av}$ are calculated from the measured numerical data where, *RMS* value of velocity fluctuation,

$$\langle u\rangle = \sqrt{\frac{\sum_{i=1}^{n}(u_i - U_{av})^2}{n}}$$

and Skewness of velocity fluctuation,

$$S_u = (\overline{u^3})/(\overline{u^2})^{3/2}.$$

The average longitudinal velocity, U_{av} is $\frac{1}{n}\sum_{i=1}^{n} u_i$ where u_i is the instantaneous longitudinal velocity.

For the numerical simulation, the computations are carried out by the incident shock Mach number of 1.60 at the inlet of the nozzle. The flow velocities behind the shock wave are determined from Rankine-Hugoniot relations and it is seen that the flow velocities behind the shock wave of Mach number, 1.60 is subsonic. For the shock wave position at the outlet of the nozzle divergent, the density fringes of the flow field are used to explain the turbulence development in the selected region. The numerical images are used to simulate with the experimental photographs and such simulation results clarify the flow phenomena like laminar flow structures, transition phenomena, flow separation line as well as viscous boundary layer separation, turbulence structure development and shock/turbulent-boundary layer interaction in the nozzle divergent which are shown in Fig. 2 and Fig. 3. The experimental photographs are taken by using the double exposure laser holographic interferometry. It is observed in the flow field images that the flow separation starts at the beginning of the divergent section and an unsteady flow field appears and the flow transition period begins. The incident shock wave at the nozzle throat is transmitted and the shock waves, transverse to the main flow, are created at the upper and lower wall surfaces of the nozzle throat and propagate towards the plane of symmetry. The two shock waves soon collide at the plane of symmetry and transmitted with each other. This can also be considered as reflections of shock waves at imaginary solid plane replacing plane of symmetry.

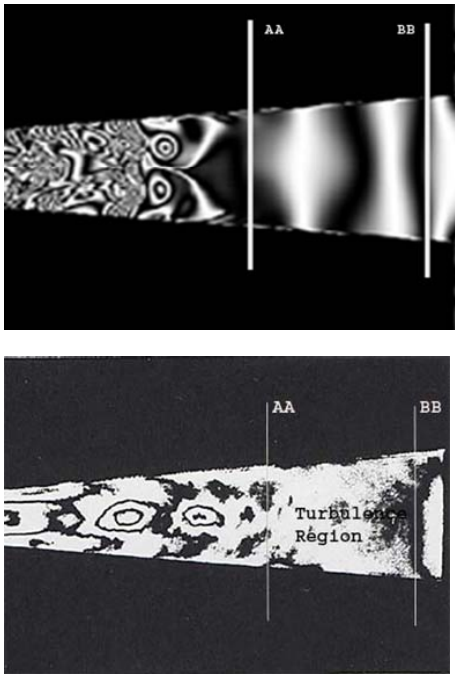

(i)

(ii)

Figure 2: (i) Numerical visualization of the divergent section of the nozzle; (ii) Experimental photograph of the divergent section of the nozzle for the propagation of shock wave of M = 1.60.

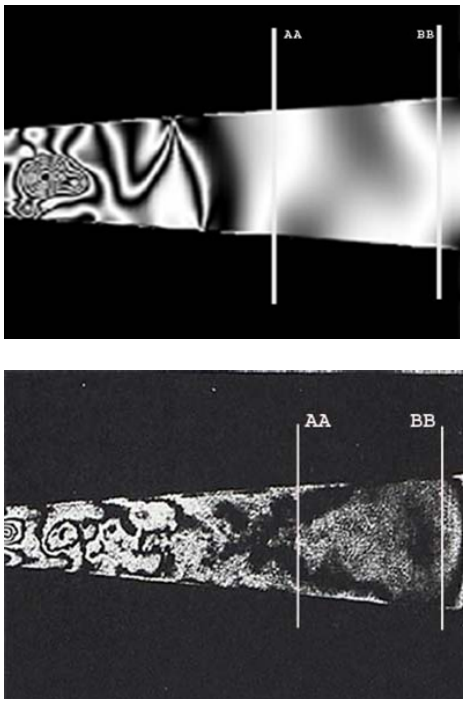

(i)

(ii)

Figure 3: (i) Numerical visualization of the divergent section of the nozzle; (ii) Experimental photograph of the divergent section of the nozzle for the propagation of shock wave of M = 1.40.

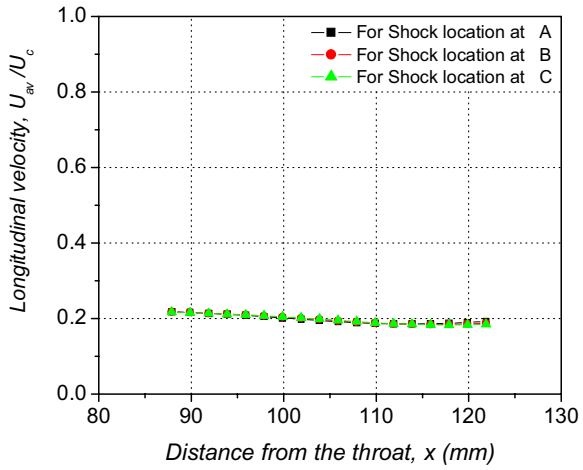

Figure 4: Longitudinal velocity profiles along the centerline of the selected region at the nozzle divergent for the different shock locations at A, B and C (Here Ms = 1.60).

The transverse shock waves repeat reflections between the nozzle walls behind the primary transmitting shock wave. Soon a secondary shock wave is generated and the flow field increases its complexity. Due to interactions with the boundary layers, the secondary shock wave is bifurcated at the wall creating bubbles of boundary layer fluid. Bifurcations of the secondary shock wave at the nozzle walls are clearly seen together with the formation of bubbles at the foot of bifurcated portions of the shock wave. The mechanism of the bifurcation was investigated by Mark [22] using a shock tube as a study of interaction of the boundary layer induced behind the incident shock wave and the shock wave reflected at the end wall. The mechanism of vortex creation and complex wave interactions in the region between the primary and the secondary shock waves are analyzed by Amann [7] and the source of the vortices is found to be the large differences in the tangential velocity at the interface.

The average longitudinal velocity, U_{av}/U_c variations are determined along the centerline of the selected region at the nozzle divergent for the different shock locations at A, B and C which are shown in Fig.4. Here U_c is the characteristics velocity. It is observed that the longitudinal velocity variations are quite reasonable for the isotropy turbulent fields and the velocity profiles, for shock movement from position A to C, are shown similar characteristics. The slight decay phenomena of the longitudinal velocity profiles appear towards outlet of the nozzle divergent which may produce homogeneous isotropic turbulent flow at outlet.

The RMS longitudinal turbulence intensity, $\langle u \rangle / U_c$ variations are determined along the centerline of the selected region at the nozzle divergent for the different shock locations at A, B and C which are shown in Fig.5. It is observed that the 2D turbulence intensity variations are quite satisfactory in the selected region and its decay phenomena towards outlet of the nozzle divergent appear due to divergent effects. It is also

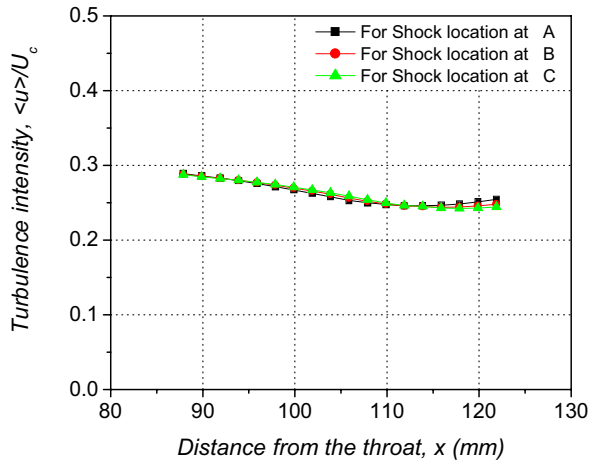

Figure 5: Turbulence intensity (<u>/U) profiles along the centerline of the selected region at the divergent section of the nozzle for the different shock locations at A, B and C (Here Ms = 1.60).

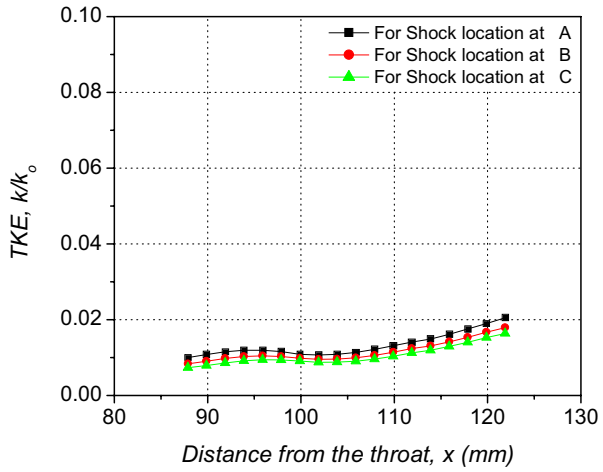

Figure 6: Turbulent kinetic energy (TKE) profiles along the centerline of the selected region at the divergent section of the nozzle for the different shock locations at A, B and C (Here Ms = 1.60).

observed that there have no effects on turbulence intensity due to the shock wave movement from position A to C which is shown in Fig. 5. The approach to isotropy of the flow was assessed by considering the skewness of the velocity fluctuations Su. From the results of Mohamed and Larue [23], it is observed that the uncertainty in their measurement of Su is 0.01, these authors concluded that the position where S_u= ±0.01 is taken for isotropic flow. According to this recommendation, the present flow appears to be isotropic at all downstream positions where the value of S_u is always less than 0.01 in the selected region.

The normalized pressure variations are determined along the centerline of the selected turbulent region at the nozzle divergent for the different shock locations and it is observed that no substantial pressure variations occur along the longitudinal direction in the selected region during the shock wave movement towards outlet of the nozzle divergent. It is also observed that no substantial RMS pressure fluctuation variations occur along the longitudinal direction in the selected region.

The turbulent kinetic energy (TKE), k/k_o variations are determined along the centerline of the selected turbulent region at the nozzle divergent for the different shock locations at A, B and C which is shown in Fig.6. It is observed that the TKE variations are reasonable for the present turbulent flow with an initially uniform TKE. The TKE evolves towards outlet of the nozzle divergent and it represents the turbulence intensity of the selected region.

The dissipation rate of TKE, $\varepsilon/\varepsilon_o$ variations are determined along the centerline of the selected turbulent region at the nozzle divergent for the different shock locations at A, B and C which is shown in Fig.7. It is observed that no substantial dissipation rate variations occur along the longitudinal direction in the selected region during shock wave movement from the outlet of the nozzle divergent. The dissipative-length scale is defined by the expression, k3/2/ε where the turbulent kinetic energy, $k = \sum_{i=1}^{n} k_i \Big/ n$ and ki is the instantaneous turbulent kinetic energy for any grid on the grid-data line and n is the number of grid on the grid-data line where the grids adjacent to the boundary are not taken into account due to viscous effect. Similarly the dissipation rate, $\varepsilon = \sum_{i=1}^{n} \varepsilon_i \Big/ n$ where εi is the instantaneous turbulent kinetic

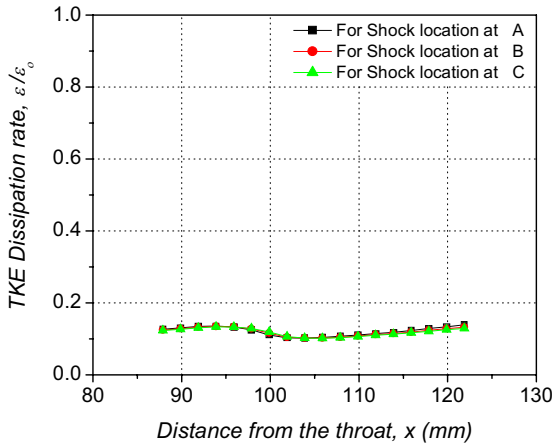

Figure 7: TKE dissipation rate profiles along the centerline of the selected region at the divergent section of the nozzle for the different shock locations at A, B and C (Here Ms = 1.60).

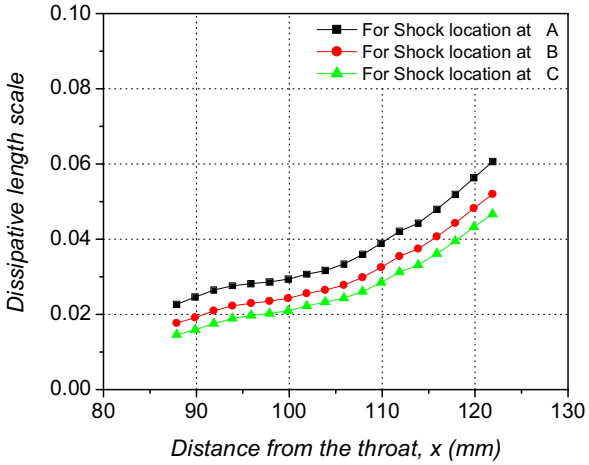

Figure 8: Dissipation length scale profiles along the centerline of the selected region at the divergent section of the nozzle for the different shock locations at A, B and C (Here Ms = 1.60).

energy dissipation rate for any grid on the grid-data line. The dissipative-length scale is determined along the centerline of the selected region at the nozzle divergent for the different shock locations at A, B and C which is shown in Fig.8. It is observed that the dissipative length scale gradually increases in the turbulent region towards outlet of the nozzle divergent. The DNS data of Lee et al. [21] and the DNS data of Hannappel and Friedrich [24] indicated that the velocity length scale and the dissipative length scale increased during expansion process. The DNS results of Lee et al. [25] had indicated a small increase of dissipative length scales through weak shock interactions. Due to stronger compressibility effects, the turbulent dissipative length scale decreases in the selected region and as decreasing the compressibility effects towards outlet of the nozzle divergent, the dissipative length scale increases.

The velocity length scale is defined by the expression, k1/2. The velocity length scale is determined along the centerline of the selected region at the nozzle divergent for the different shock locations. It is observed that no substantial velocity length scale variations occur along the longitudinal direction in the selected region during the shock wave movement from the outlet of the nozzle divergent.

IV. Conclusions

An investigation has been carried out for the shock induced turbulence in the nozzle flow. Experimental photographs are used to compare with numerical images for density fringes of the flow field and it is concluded that proper visualizations are performed by both experimentally and numerically to visualize some phenomena, like shock/turbulent boundary layer interaction, flow separation, Mach reflection and fully developed turbulent field. It is observed that the simulation results have the good agreements with the experimental results. Due to acceleration of the shock speed at the divergence part, tremendous viscous flow separations as well as shock induced turbulent flow field gradually appears towards outlet of the nozzle divergent. In the present computation, 2D turbulence intensity variations are determined in the selected region along the longitudinal direction of the nozzle divergent and it is observed that the turbulence decay appears because of decreasing the effects of shock/boundary layer interaction towards outlet. The TKE evolves along the longitudinal direction of the nozzle divergent and the flow expansion occurs at nozzle divergent and it affects the TKE variations. The expansion/compression affects the turbulent length scale and the dissipative length scale increases towards the outlet of the nozzle divergent.

References

[1] Wilmoth RG and Leavitt LD. (1987) Navier Stokes predictions of multifunction nozzle flows. SAE Trans. 96(6), 6.865–6.879.
[2] Hamed A and Vogiatzis C. (1997) Overexpanded two-dimensional convergent-divergent nozzle flow simulations, Assessment of Turbulence Models. J. Propulsion Power 13(3), 444–445.
[3] Hamed A and Vogiatzis C. (1998) Overexpanded two-dimensional convergent-divergent nozzle flow performance, effects of three dimensional flow interactions. J. Propulsion Power 14(2), 234–440 (1998)
[4] Hunter CA. (1998) Experimental, theoretical and computational investigation of separated nozzle flows. AIAA Paper 98-3107.
[5] Prodromou P and Hillier R. (1992) Computation of unsteady nozzle flows. Proc. of the 18th ISSW Sendai, Japan, II:1113–1118.
[6] Igra O, Wang L, Falcovitz J and Amann HO. (1998) Simulation of the starting flow in a wedge-like nozzle. Shock Waves 8:235–242.
[7] Amann HO. (1969) Experimental study of the starting process in a reflection nozzle. Phys. Fluids Supplement 12:150–153.
[8] Jacobs PA. (1991) Simulation of transient flow in a shock tunnel and a high Mach number nozzle. NASA CR 187606.
[9] Tokarcik-Polsky S and Cambier JL. (1994) Numerical study of transient flow phenomena in shock tunnels. AIAA Journal 32:971–978.
[10] Saito T, Timofeev EV, Sun M and Takayama K. (1999) Numerical and experimental study of 2-D nozzle starting process. Paper 4090, in the Proceedings of the 22nd ISSW, Imperial College, London, UK, July 18–23.
[11] Chen CL, Chakravarthy SL and Hung CM. (1994) Numerical Investigation of Separated Nozzle Flows. AIAA Journal,Vol. 32; pp. 1836-1843.
[12] Nasuti F and Onofri M. (1994) Transient Flow analysis of nozzle start-up by a shock fitting technique. Unsteady Flows in Aero-propulsion, edited by W. Ng. D. Fant and L. Povinelli, AD-40:127–135, ASME, New York, pp. 127–135.
[13] Nasuti F and Onofri M. (1998) Viscous and Inviscid Vortex Generation during Startup of Rocket Nozzles. AIAA Journal, Vol. 36; pp. 809–815.
[14] Seegmiller HL, Marvin JG and Levy LL Jr. (1978) Steady and Unsteady Transonic Flow, AIAA Journal 16 (12); pp. 1262.
[15] Chen CP, Sajben M and Kroutil JC. (1979) Shock Wave Oscillations in a
Transonic Diffuser Flow, AIAA Journal 17 (10); pp. 1076.
[16] Liou MS and Coakley TJ. (1984) Numerical Simulations of Unsteady. Transonic Flow in Diffusers, AIAA Journal 22 (8); pp. 1139.
[17] Arnone A, Liou MS and Povinelli LA. (1995) Integration of Navier-Stokes
equations using dual time stepping and a multigrid method, AIAA Journal 33 (6); pp. 985.
[18] Gerolymos GA, Vallet I, B¨olcs A and Ott P. (1996) Computation of unsteady three-dimensional transonic nozzle flows using k-epsilon turbulence closure, AIAA Journal 34 (7); pp. 1331.
[19] Bron O, Ferrand P and Fransson T 2002 Proc. 9 th Int. Symp. on Transport Phenomena and Dynamics of Rotating Machinery, Honolulu, Hawaii, pp. 1–9.
[20] Setoguchi T, Matsuo S and Kim H D 2003 Proc. Symp. on Shock Waves, Japan, pp. 49–52.

[21] Lee S, Lele SK and Moin P. (1993) Direct numerical simulation of isotropic turbulence interacting with a weak shock wave. Journal of Fluid Mechanics, Vol. 251; pp. 533-62.
[22] Mark G. (1958) The interaction of a reflected shock wave with the boundary layer in a shock tube. NACA TM 1418.
[23] Mohamed MS and LaRue JC. (1990) The decay of power law in grid-generated turbulence. Journal of Fluid Mechanics; Vol. 219: p-195.
[24] Hannappel R and Friedrich R. (1995) Direct numerical simulation of a Mach 2 shock interacting with isotropic turbulence. Appl. Sci. res. Vol. 54; pp. 205-21.
[25] Lee S, Lele SK and Moin P. (1994) Interaction of isotropic turbulence with a strong shock wave. AIAA paper 94-0311. Dept. Mech. Eng., Stanford Univ., CA.